In situ synchrotron diffraction of pressure-induced phase transition in $DyPO_4$ under variable hydrostaticity

Jai Sharma [1], Matthew Musselman [1], Bianca Haberl [2] and Corinne E. Packard [1,*]

[1] *Colorado School of Mines, Golden, Colorado 80401, USA*

[2] *Neutron Scattering Division, Neutron Sciences Directorate, Oak Ridge National Laboratory, Oak Ridge, Tennessee 37831, USA*

(Received 11 January 2021; revised 15 April 2021; accepted 26 April 2021; published 12 May 2021)

In situ synchrotron x-ray diffraction was conducted on polycrystalline $DyPO_4$ to elucidate the details of the pressure-induced transition from the xenotime polymorph to the monazite polymorph. We used three different pressure-transmitting media (neon, a 16:3:1 methanol-ethanol-water mixture, and potassium chloride) to investigate the effect of hydrostaticity on the phase behavior. Specifically, our data clearly show a hydrostatic onset pressure of the xenotime-monazite transition of 9.1 GPa, considerably lower than the 15.3 GPa previously determined by Raman spectroscopy. Based on (quasi)hydrostatic data taken in a neon environment, third-order Birch-Murnaghan equation-of-state fits give a xenotime bulk modulus of 144 GPa and a monazite bulk modulus of 180 GPa (both with pressure derivatives of 4.0). Structural data and axial compressibilities show that $DyPO_4$ is sensitive to shear and has an anisotropic response to pressure. More highly deviatoric conditions cause the onset of the transition to shift to pressures at least as low as 7.0 GPa. We attribute early transition to shear-induced distortion of the PO_4 tetrahedra. Our characterization of the high-pressure behavior of $DyPO_4$ under variable hydrostaticity is critical for advancing rare earth orthophosphate fiber coating applications in ceramic matrix composites and may inform future tailoring of phase composition for controlled shear and pressure applications.

DOI: 10.1103/PhysRevB.103.184105

I. INTRODUCTION

Rare earth orthophosphates ($REPO_4$) are a burgeoning class of ceramics, most of which transition to other phases under pressure [1–3]. In equilibrium at atmospheric pressure, heavier compositions (RE = Tb-Lu, Sc, and Y) adopt the xenotime (tetragonal, $I4_1/amd$) structure, while lighter compositions (RE = La-Gd) adopt the monazite (monoclinic, $P2_1/n$) structure [4]. At high pressures, xenotime compositions can transition into monazite or other structures. This polymorphism has spurred recent interest in $REPO_4$ for ceramic matrix composite (CMC) applications, where the xenotime-monazite transition offers the possibility of additional plasticity and toughening mechanisms in oxide-oxide CMCs [5,6]. Hay *et al.* [4,6] showed that $DyPO_4$ (among other xenotime) fiber coatings deflect cracks and result in lower fiber push-out stresses than monazite $LaPO_4$ coatings.

Figure 1 shows the xenotime and monazite structures of $DyPO_4$, and the mechanism of transition is as follows: under compression, Dy-O bonds are distorted to the point of reconfiguration (the RE coordination number increases from 8 to 9), while the PO_4 groups (gray tetrahedra) are effectively rigid [7,8]. This description is widely accepted for all $REPO_4$ compositions that undergo the xenotime-monazite transition.

Most xenotime $REPO_4$ transitions have been extensively investigated using *in situ* diamond anvil cell (DAC) Raman spectroscopy (RS) and x-ray diffraction (XRD) techniques. For $TbPO_4$, in their RS study, Tatsi *et al.* [9] reported a high-pressure polymorph that was likely monazite. In their XRD study, López-Solano *et al.* [10] then confirmed that this polymorph was of the monazite structure and provided detailed structural information including an equation of state (EoS) for both polymorphs. In their single-crystal XRD work, Gomis *et al.* [11] showed that $HoPO_4$ and $TmPO_4$ transition to the monazite structure and gave elastic constants and an EoS for each material in the xenotime phase. In their synchrotron XRD study, Lacomba-Perales *et al.* [3] showed the xenotime-monazite transition in $ErPO_4$ and YPO_4 and gave an EoS for both polymorphs. However, all xenotime compositions do not transition to monazite; Zhang *et al.* [12,13] reported that $YbPO_4$, $LuPO_4$, and $ScPO_4$ transition to the scheelite (tetragonal, $I4_1/a$) structure.

Similar insight into the high-pressure phase behavior of $DyPO_4$ has yet to be reported, though significant steps have been taken. Using *in situ* DAC RS, Musselman *et al.* [14] and Stavrou *et al.* [15] reported $DyPO_4$ transition onset pressures (P_{onset}) of 15.3(9) GPa and 13 GPa, respectively. They both attribute emergent Raman peaks at these pressures to a polymorph that takes on the monoclinic, monazite structure. The determination by Musselman *et al.* [14] is based on peaks emerging at locations consistent with monazite $TbPO_4$ peaks. Stavrou *et al.* [15] further claim that monazite $DyPO_4$ transforms to scheelite at higher pressures ~30 GPa. This xenotime-monazite-scheelite transition pathway is consistent with that of neighboring xenotime $REPO_4$ [15]. Other ABO_4 compounds like alkaline-earth phosphates are stable in the monazite structure up to at least 30 GPa [3]. Very recently, Heuser *et al.* [16] synthesized metastable $DyPO_4$ in the monazite structure. While literature on the xenotime and

*Corresponding author: cpackard@mines.edu

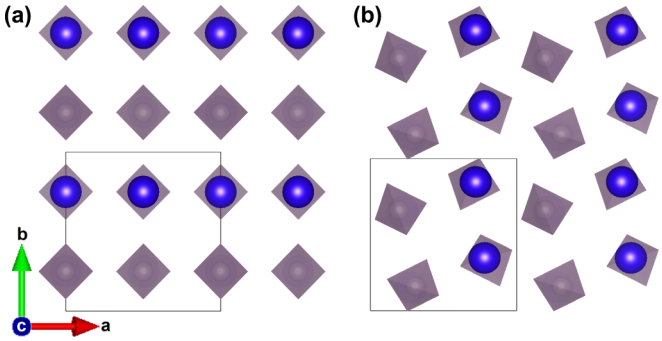

FIG. 1. [001] views of the (a) xenotime and (b) monazite phases of dysprosium orthophosphate $DyPO_4$. Violet spheres represent Dy^{3+} cations, gray tetrahedra represent PO_4^{3-} groups, and the boxes represent one unit cell. The apparent 90 ° rotation of monazite with respect to xenotime is merely a result of the monoclinic cell setting of monazite.

monazite $DyPO_4$ polymorphs exists, the fundamental thermodynamics and kinetics of the transition are not fully established.

Moreover, the impact of hydrostaticity on the onset of the $DyPO_4$ transition has yet to be reported. It is well documented that higher shear components often lower P_{onset}, and Lacomba-Perales *et al.* [3] came to similar conclusions when comparing their YPO_4 findings to previous work [17]. Although the effect of hydrostaticity has yet to be systematically studied for $REPO_4$, it has been studied in other ABO_4 compounds. For example, Santamaría-Pérez *et al.* [18] conducted a systematic study for orthorhombic $BaSO_4$. Under less hydrostatic conditions, they found that transition began earlier and that the pressure range of phase coexistence was wider. Assessing the impact of hydrostaticity on the $DyPO_4$ transition is critical as structural applications like CMCs involve a significant degree of deviatoric stress in addition to hydrostatic pressure.

This paper employs *in situ* DAC synchrotron XRD to directly and quantitatively interrogate the $DyPO_4$ structure and phase behavior. To apply pressure with varying degrees of hydrostaticity, three pressure-transmitting media (PTM) were used: neon, a 16:3:1 methanol-ethanol-water mixture, and the soft salt KCl. Diffraction patterns were used to determine P_{onset}, calculate axial compressibilities, and develop EoSs for the xenotime and monazite phases. Our findings show a quasihydrostatic P_{onset} of 9.1(1) GPa, much lower than the previously reported RS-based value of 15.3(9) GPa [14]. In addition, deviatoric stresses induced by the solid PTM KCl trigger an even earlier $DyPO_4$ transition at least as low as 7.0 GPa. Independent of hydrostaticity (i.e., with all PTM used here), experiments reveal a wider pressure range of xenotime-monazite coexistence than was indicated by RS, suggesting that this transition is kinetically limited. Axial data from the quasihydrostatic experiments show that $DyPO_4$ response to pressure is anisotropic. Third-order Birch-Murnaghan EoS fits yield a xenotime bulk modulus ($B_{0,X}$) of 144(1) GPa with a pressure derivative of 4.0 and monazite bulk modulus ($B_{0,M}$) of 180(11) GPa with a pressure derivative of 4.0.

II. EXPERIMENTAL DETAILS

Phase-pure xenotime $DyPO_4$ powder was obtained via precipitation reaction involving $Dy(NO_3)_3 \cdot 5H_2O$ ($\geqslant$99.9% RE oxide basis, Alfa Aesar) precursor and H_3PO_4 (85% w/w aqueous solution, Alfa Aesar) and subsequent calcination. Details of these two steps are described elsewhere [14]. *In situ* DAC XRD was conducted at room temperature at beamline 16-ID-B, HPCAT, Advanced Photon Source, Argonne National Laboratory. For all experiments, 301 stainless steel gaskets were drilled with the HPCAT laser micromachining system [19], and two-dimensional diffraction patterns were collected with the PILATUS 1M-F detector. The x-ray beam spot size (full width at half maximum) was ~4 μm (vertical) by 6 μm (horizontal). These experiments were conducted over two synchrotron beam trips, resulting in slight differences in experimental details (such as beam wavelength). These details as well as experimental details of the DACs used are listed in Table I.

DAC preparation involved loading the $DyPO_4$ powder sample and the pressure marker (Au or ruby) into the gasket chamber. Great care was taken that the sample did not bridge the anvils or gasket walls for best hydrostatic conditions. Three different PTM were used: neon, 16:3:1 methanol-ethanol-water mixture, and KCl. The 16:3:1 methanol-ethanol-water mixture is hereafter referred to as the "mixture." In the case of KCl and the mixture, after a ruby was added to the sample, the PTM was added, and the cell was closed and sealed. In the neon experiment, neon gas was loaded using the GSECARS gas membrane loading system [20]. The cell was then set up with a dual membrane system for (de)compression rate control [21]. Adding the can assembly for membrane compression to the already gas-loaded cell resulted in an inadvertent initial pressure jump to ~4 GPa before placing the cell on the beamline. There were no reported $DyPO_4$ phase transitions below ~4 GPa (as corroborated by our mixture and KCl experiments); therefore, the initial jump in the neon experiment does not preclude any material insight. The beamline's PACE 5000 pressure controlling system was then used to pressurize the cell during the experiment [21]. Pressure was determined from the unit cell volume and third-order Birch-Murnaghan EoS of gold (>99.96% metals basis, Alfa Aesar) [22,23].

The mixture and KCl PTM experiments used an Almax easyLab plateDAC (Almax easyLab Inc., Cambridge, MA) and ruby chips (Almax easyLab Inc., Cambridge, MA) as pressure markers. The cell was pressurized by manual crank, and pressure was determined using ruby R1 fluorescence [24]. Other distinct experiment parameters are shown in Table I. Pressures derived from ruby fluorescence are presented without error estimates, as only nominal values were recorded. Although these two experiments used a different pressure marker than the neon experiment, any systematic error in pressure scales was likely minimal as the gold EoS used in this study was calibrated against the ruby fluorescence method [22]. In addition, the ruby scale used in this study was also used in the Raman study of Musselman *et al.* [14], ensuring pressure scale consistency with prior Raman work.

XRD pattern integration, masking, and background subtraction were performed using Dioptas [25]. Pattern fitting

TABLE I. Experimental details for each of the three PTM experiments.

PTM	Beam λ (Å)	No. Scans	Exposure time (s)	Loading rate (MPa/s)	Pressure marker	Gasket hole thickness, diameter (μm)	Culet diameter (μm)	DAC type	P_{max} (GPa)
Neon	0.48595	74	1	1.8	Gold powder	~40, ~110	250	Symmetric	14.8
Mixture	0.40663	26	5	1.1	Ruby chips	110, 250	500	Almax easyLab plate	14.2
KCl	0.40663	16	7.5	1.6	Ruby chips	68, 180	380	Almax easyLab plate	12.6

was then performed using X'Pert HighScore Plus [26]. This software fits monazite using the $P2_1/c$ cell setting as a default. Although both the $P2_1/c$ and $P2_1/n$ cell settings are valid descriptions of monazite (space group No. 14), fitted lattice parameters were converted to the $P2_1/n$ cell setting for ease of comparison to literature. The atmospheric-pressure volume of xenotime $DyPO_4$ was calculated from a synchrotron scan ($\lambda = 0.48595$ Å) at 0 GPa (before any compression) using a plate DAC with no PTM. The zero-pressure bulk modulus (B_0) of $DyPO_4$ and its pressure derivative (B_0') were determined by fitting volume vs pressure data to the third-order Birch-Murnaghan EoS with the EoSFit7-GUI program [27]. Xenotime EoS and axial compressibility fits used scans with $P < P_{onset}$, while monazite EoS and axial compressibility fits used scans with $P \geqslant P_{onset}$. For all other computation involving derived data (e.g., unit cell volume, gold-based pressure, cell setting conversion), Python was used to propagate error, and a covariance of zero was assumed.

III. RESULTS

All three experiments have similar quasistatic loading rates (see Table I and Fig. S1 in the Supplemental Material [28]) despite the varying mode of pressure application. Thus, we do not attribute differences among datasets to kinetic effects. The LeBail fitting approach is used instead of traditional Rietveld structure refinement to accommodate the significant preferred orientation present in all scans of all experiments (Fig. S2 in the Supplemental Material [28] illustrates a representative example) [29]. Preferred orientation appears due to the small spot size of the beam with respect to the grain sizes of the present sample (sampling a finite number of grains). It is thus also observed for the neon loading despite the better hydrostaticity of neon. The xenotime, monazite, neon, and KCl structures used for pattern fitting were determined by Milligan *et al.* [30], Heuser *et al.* [16], Finger *et al.* [31], Hemley *et al.* [32], Klotz *et al.* [33], and Froyen and Cohen [34], respectively.

The zero-pressure xenotime unit cell volume ($V_{0,X}$) used for normalization in Fig. 2 is 289.39(2) Å^3. The dashed lines show $DyPO_4$ P_{onset} values of 9.1(1), 9.3, and 7.0 GPa when pressurized with the neon, mixture, and KCl PTM, respectively. The respective $DyPO_4$ volume contractions at P_{onset} are 6.96(3), 7.17(3), and 8.75(3)%. Figures 3–5 show that all XRD peaks drift to higher Q and become more diffuse due to uniform and nonuniform strain, respectively. Transformation onset is determined by visual inspection of individual XRD patterns (see Fig. S3 in the Supplemental Material [28]), not by judging color in the following contour plots [Figs. 3(a), 4(a), and 5(a)]. Visual inspection involves plotting the square root of intensity against Q to ensure that emerging peaks are not overlooked due to their extremely low intensity. Any given pattern is fit with both the xenotime and monazite phases only when visual inspection of that pattern reveals intensity at Q values consistent with monazite peaks. In the neon experiment, the (110), (002), and (02$\bar{1}$) monazite peaks are used to mark P_{onset}, as they are the first monazite peaks to emerge and do not overlap with xenotime signal. In the mixture and KCl experiments, the (002) peak does not appear because of variation in preferred orientation between experiments. Therefore, only the (110) and (02$\bar{1}$) monazite peaks are used to mark P_{onset} in these experiments, as shown in Figs. S3(b) and S3(c) in the Supplemental Material [28]. All expected xenotime peaks appear in low-pressure patterns and persist after P_{onset} for all experiments. In addition, all major monazite peaks are observed at high pressure. Minor monazite peaks at $Q > 3$ Å^{-1} are more difficult to verify, as they often overlap with each other or stronger PTM, pressure marker, or xenotime peaks.

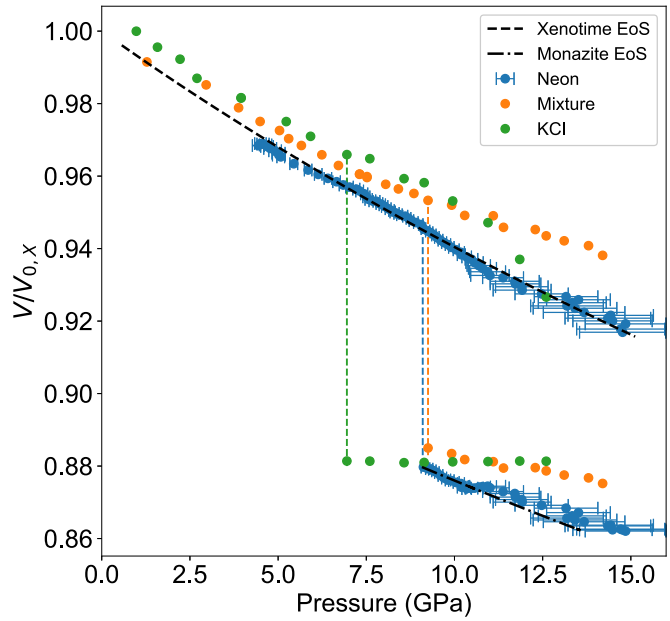

FIG. 2. $DyPO_4$ unit cell contraction during compression under neon, mixture, and KCl pressure-transmitting media (PTM). Volumes are normalized by the xenotime volume at 0 GPa, $V_{0,X}$ (in which X denotes xenotime). Vertical dashed lines indicate P_{onset}. For each PTM, the cluster at the top of the dashed line represents xenotime, while the cluster at the bottom of the dashed line represents monazite. Error bars represent standard deviation. In mixture and KCl datasets, pressure was recorded as a nominal value. Volume error bars for all datasets are within the symbols. Black dashed curves represent equation of state (EoS) fits of neon data performed with a fixed bulk modulus pressure derivative (see Table II).

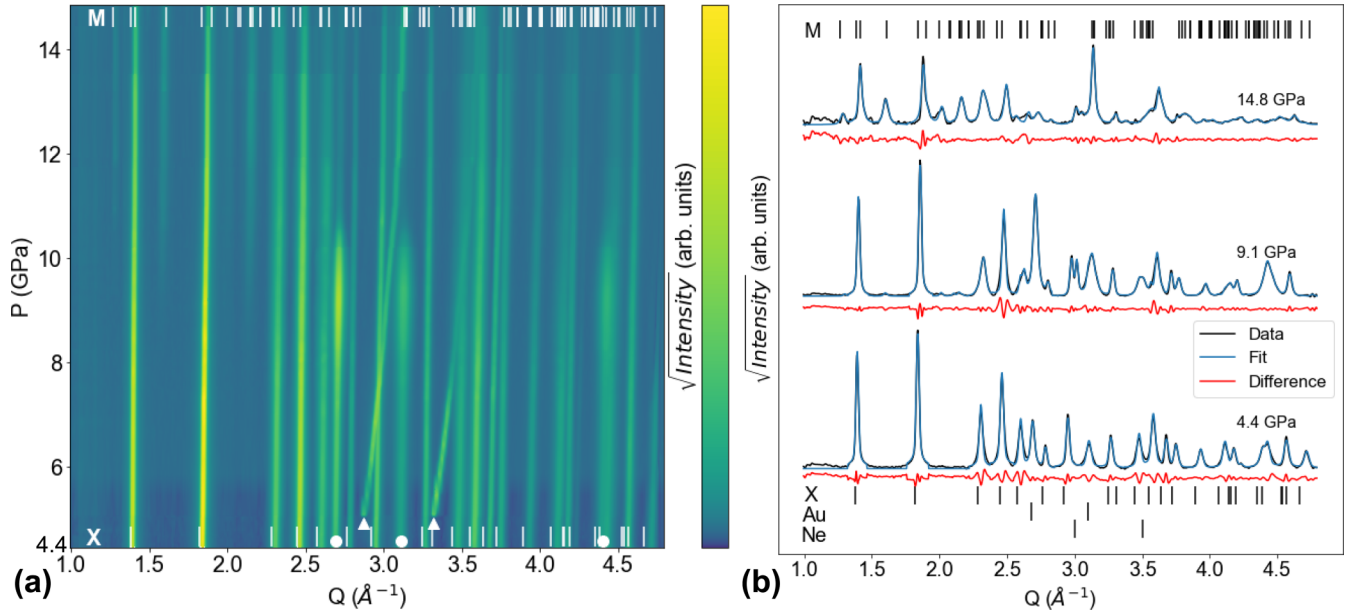

FIG. 3. Neon dataset. X ticks show a low-pressure xenotime reference pattern [30], while the M ticks show a monazite fit. (a) Contour plot showing all x-ray diffraction (XRD) patterns. Monazite peaks emerge at 9.1(1) GPa. Circles and triangles denote the gold and neon peaks, respectively. (b) Select XRD patterns (initial, transition onset, final) and their LeBail fits.

Figures 3(a) and 3(b) show XRD pattern evolution and LeBail fit quality (at P_{initial}, P_{onset}, and P_{final}), respectively, in the neon experiment. The first scan in this experiment is at a modestly high pressure of 4.4 GPa due to the gas membrane can setup and features xenotime and gold [circles in Fig. 3(a)] peaks. Nonxenotime peaks first emerge at 5.0 GPa; this corresponds to the crystallization of neon as reported in the literature [31]. This is noteworthy, as the conditions shift from hydrostatic (in liquid Ne) to quasihydrostatic (in solid Ne) at this point in pressure. Neon peaks shift more dramatically than the other materials' peaks because neon is the most compressible material in the DAC [32]. The first discernible monazite peaks emerge at 9.1(1) GPa and are located at $Q =$ 1.59, 2.02, and 2.14 Å^{-1}; these are the (110), (002), and (02$\bar{1}$) reflections, respectively. In the P_{onset} scan, the refined monazite lattice parameters are $a = 6.150(1)$ Å, $b = 6.627(1)$ Å, $c = 6.384(1)$ Å, and $\beta = 99.60(1)^\circ$. Note that, ~10 GPa, the gold signal becomes extremely weak, likely due to gold grains

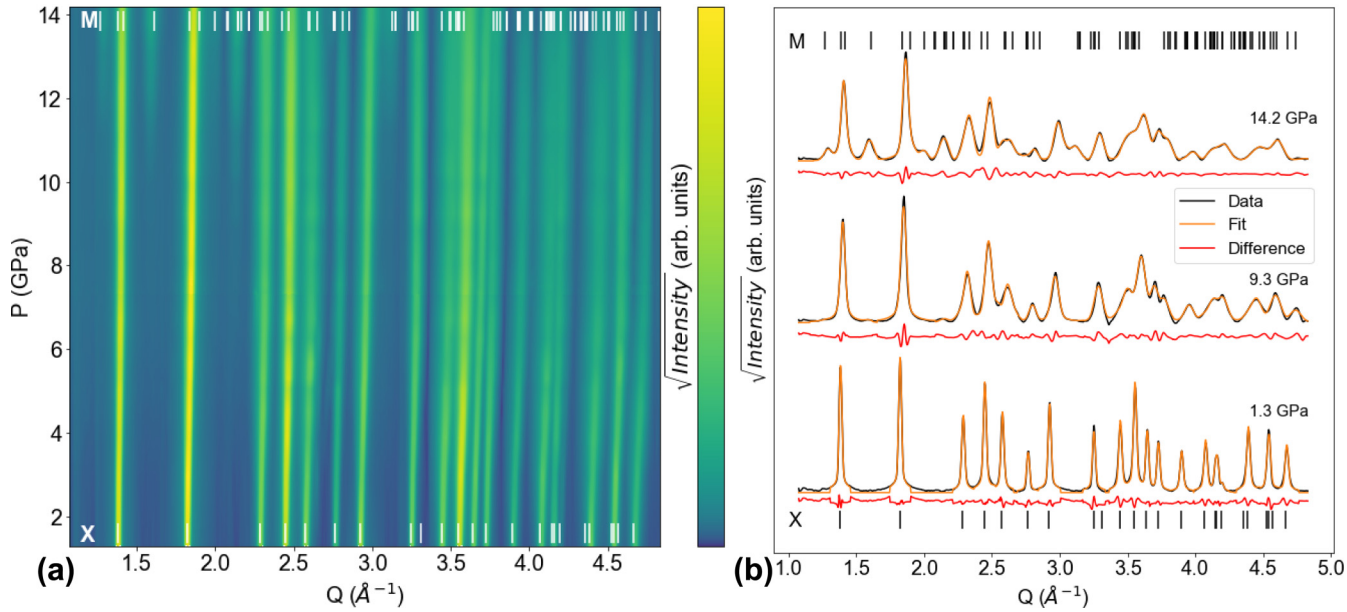

FIG. 4. Mixture dataset. X ticks show a low-pressure xenotime reference pattern [30], while the M ticks show a monazite fit. (a) Contour plot showing all x-ray diffraction (XRD) patterns in ramp. Monazite peaks emerge at 9.3 GPa. (b) Select XRD patterns (initial, transition onset, final) and their LeBail fits.

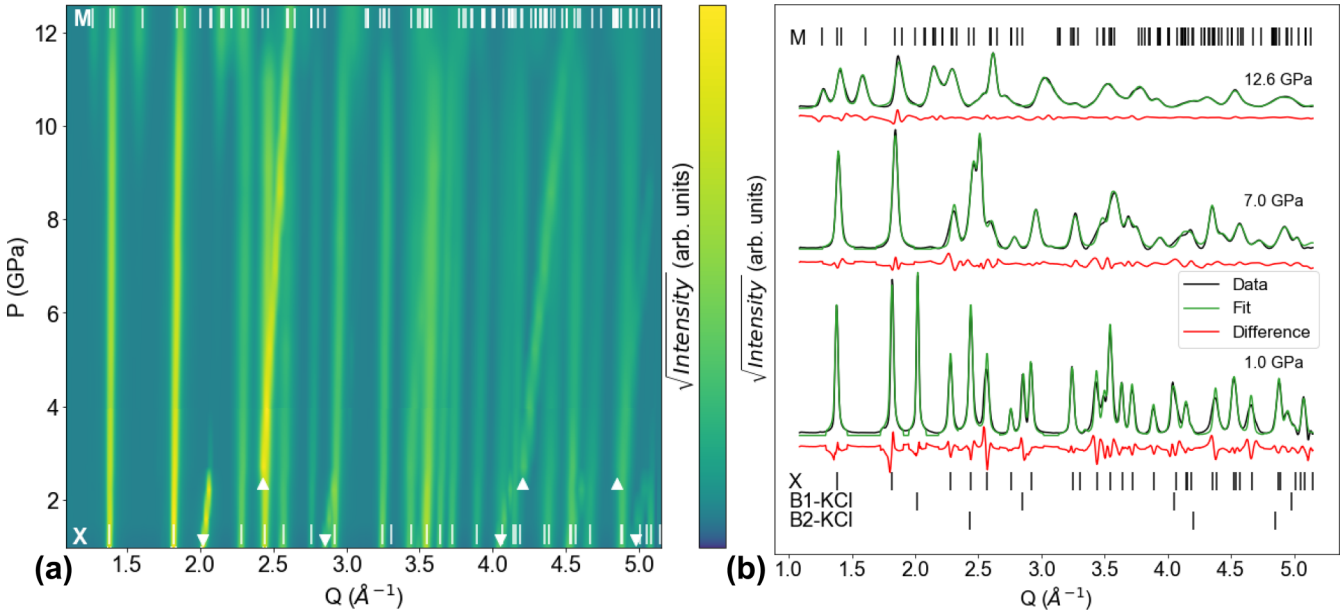

FIG. 5. KCl dataset. X ticks show a low-pressure xenotime reference pattern [30], while the M ticks show a monazite fit. (a) Contour plot showing all x-ray diffraction (XRD) patterns in ramp. Inverted and upright triangles represent the B1 and B2 phases of KCl, respectively. Monazite peaks emerge at 7.0 GPa. (b) Select XRD patterns (initial, transition onset, final) and their LeBail fits.

shifting out of the beam spot after the onset of the xenotime to monazite transition. In addition, the weak gold peaks start to overlap with stronger xenotime and now-solidified neon peaks. This overlap makes precisely locating the gold peak much more difficult. As a result, the uncertainty in the fitted gold lattice parameter increases dramatically. Since pressure is determined as a function of gold lattice parameter, the pressure uncertainty also increases dramatically.

Figures 4(a) and 4(b) show XRD pattern evolution and LeBail fit quality (at P_{initial}, P_{onset}, and P_{final}), respectively, in the mixture experiment. The first scan at 1.3 GPa only shows xenotime peaks as the mixture PTM remains a liquid at this pressure and is indiscernible. The first discernible monazite peaks emerge at 9.3 GPa; these are located at $Q =$ 1.59 and 2.13 Å^{-1} and correspond to the (110), and (02$\bar{1}$) reflections, respectively. In the P_{onset} scan, the refined monazite lattice parameters are a = 6.159(1) Å, b = 6.611(1) Å, $c = 6.425(1)$ Å, and $\beta = 99.50(1)^\circ$. It is noteworthy that this transition commences prior to the freezing of the mixture; this means the mixture remains hydrostatic at P_{onset}. At ∼10.5 GPa (the mixture's effective hydrostatic limit), the mixture undergoes a glass transition into an amorphous solid phase that contributes no XRD peaks [33].

Figures 5(a) and 5(b) show XRD pattern evolution and LeBail fit quality (at P_{initial}, P_{onset}, and P_{final}), respectively, in the KCl experiment. The first scan shows peaks from xenotime $DyPO_4$ and B1-KCl (inverted triangles), which takes on a NaCl-type structure. At ∼2.7 GPa, B1-KCl transitions to B2-KCl (upright triangles), taking on a CsCl-type structure [34]. The KCl transition does not seem to affect the phase behavior of $DyPO_4$ in the KCl transition regime. Both sets of KCl phases' peaks have higher slope than $DyPO_4$'s peaks because both KCl phases are more compressible than $DyPO_4$ [34]. In marked contrast to the neon and mixture experiments, the first discernible monazite peaks emerge early at 7.0 GPa and are located at $Q = 1.58$ Å^{-1} and 2.12 Å^{-1}; these are the (110) and (02$\bar{1}$) reflections, respectively. In the P_{onset} scan, the monazite lattice parameters are $a = 6.165(1)$ Å, $b = 6.6673(5)$ Å, $c = 6.407(1)$ Å, and $\beta = 101.842(3)^\circ$. Although these uncertainties appear quite small, several checks on the LeBail fits did not change the outcome.

Figure 6 plots the $DyPO_4$ lattice parameters from the LeBail fits for all three PTM. Xenotime lattice parameters (a_x and c_x) steadily decrease during loading and have no apparent discontinuity or change in slope at P_{onset} across all PTM. Monazite lattice parameters (a_M, b_M, c_M, and β_M) are less sensitive to pressure than xenotime parameters, and the differences among the values of a_M, b_M, and c_M are roughly the same across PTM. Here, β_M (shown in Fig. 6 insets) spans similar ranges in the neon and mixture datasets but spans a much higher and tighter range in the KCl dataset. Contrary to xenotime trends, monazite lattice parameter trends have some slight but statistically significant irregularities. Soon after P_{onset} in the neon dataset [Fig. 6(a)], a_M and b_M experience temporary dips, and β_M experiences a temporary bump. After ∼10 GPa in the mixture dataset [Fig. 6(b)], the a_M trend becomes steeper, and the b_M and c_M trends become nonmonotonic. It is also notable that the monazite unit cell volume does not contract upon compression in the KCl dataset, consistent with a high shear component present in the experiment.

IV. DISCUSSION

This paper clearly shows that $DyPO_4$ transitions directly from the xenotime (tetragonal, $I4_1/amd$) to the monazite (monoclinic, $P2_1/n$) polymorph with no intermediate phase regardless of PTM. This result differentiates $DyPO_4$ from neighboring $REPO_4$ compositions (e.g., $TbPO_4$ and $Gd_xDy_{1-x}PO_4$), which exhibit an intermediate anhydrite phase [4]. No errant XRD peaks are observed in this paper,

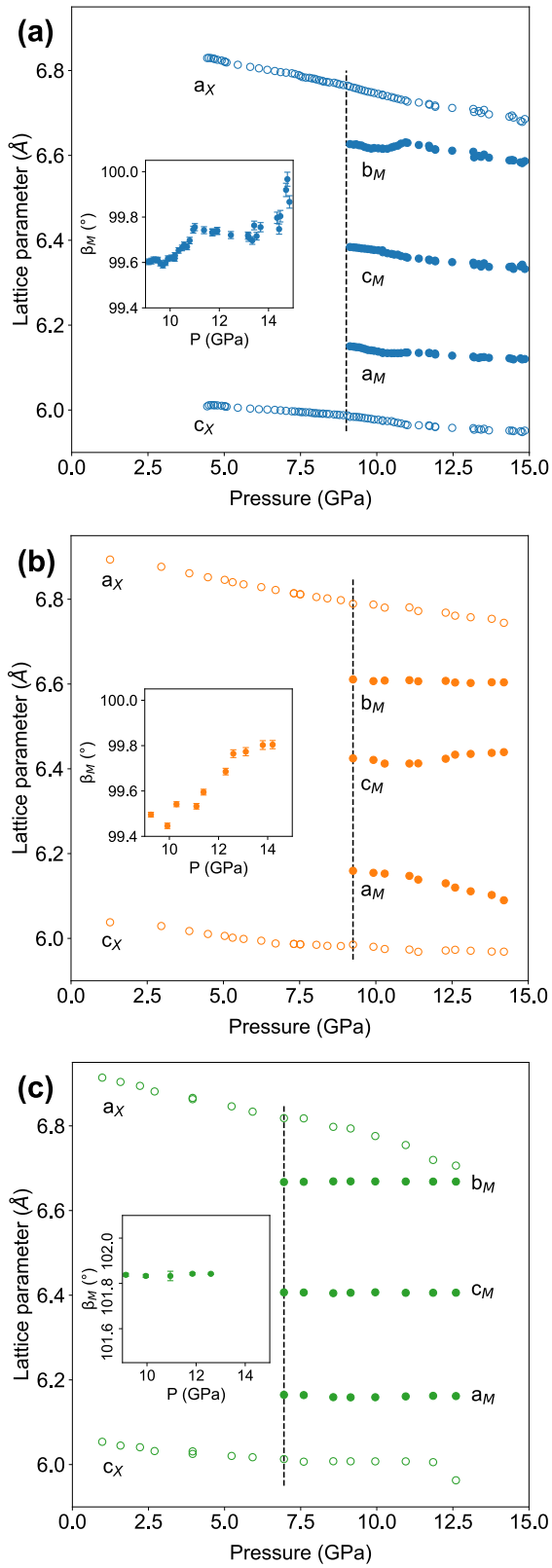

FIG. 6. Pressure dependence of xenotime and monazite lattice parameters from the (a) neon, (b) mixture, and (c) KCl datasets. Dashed lines indicate P_{onset}. Lattice parameter error bars are within the symbol size. Insets show the monazite beta angle with standard deviation error bars. Across pressure-transmitting media (PTM), consistent *y*-axis ranges for the panels and for the insets enable slope comparison.

and forcing an anhydrite phase into the LeBail fits worsens fit quality. Moreover, the revised Bastide stability diagram of Hay *et al.* [4] shows that $DyPO_4$ is too far from the xenotime-anhydrite-monazite triple point. Once the monazite polymorph commences nucleation, there is a notably large pressure range of xenotime-monazite coexistence for all PTM. In fact, the upper limit of the pressure range of coexistence remains unknown as the xenotime signal is still present in the final (highest pressure) scans taken herein. Phase fraction estimates from Rietveld refinements (see Fig. S6 in the Supplemental Material [28]) show that KCl promotes more significant monazite formation than neon and the mixture in addition to lowering the onset pressure, providing evidence that shear lowers the barrier to phase transition or otherwise increases the transformation kinetics in this system. In their $BaSO_4$ study, Santamaría-Pérez *et al.* [18] showed a wider coexistence range under less hydrostatic media, though different mechanisms and different transformation kinetics are expected in barite. Other $REPO_4$ compositions are also reported to have significant ranges of phase coexistence [3,10]. This coexistence, however, violates Gibb's phase rule [35]. For a single-component system in which temperature is fixed and pressure is the only degree of freedom, only one phase is thermodynamically allowed to exist; therefore, the observation of a significant xenotime-monazite coexistence range even under hydrostatic conditions in this paper and others suggests that the transition is kinetically limited. It would be interesting to consider future studies with variable ramp rate and at elevated temperature, but this is outside the scope of this paper.

Another significant finding is that the XRD-based P_{onset} of 9.1(1) GPa is far lower than RS-based values of 15.3(9) reported by a subset of the authors of this paper [14] and 13 GPa reported by Stavrou *et al.* [15]. The large difference between RS- and XRD-based P_{onset} values is unexpected, as the RS-XRD discrepancy in $TbPO_4$ (an adjacent composition) is only 0.3 GPa [9,10]. Taking a closer look at the Raman spectra of Musselman *et al.* [14] provides a likely explanation for this 6.2 GPa gap. In that study, P_{onset} is marked by the appearance of small, distinct Raman bands representing almost all the optical modes of monazite. These modes harden with increasing pressure. Extrapolating monazite mode linear fits to lower pressures reveals that most of these modes fall within the broad peaks of xenotime modes at ~9 GPa (see Fig. S4 in the Supplemental Material [28]). In other words, monazite Raman modes may exist in the ~9 GPa spectrum as weak shoulders or weak tails of xenotime Raman modes, but the poor signal-to-noise ratio of RS prevents unambiguous interpretation of these weak features as monazite signal. In their high pressure RS study of $DyPO_4$, Stavrou *et al.* [15] report a xenotime-monazite P_{onset} of 13 GPa, which presumably suffers from the same peak overlap; however, the underlying Raman spectra have yet to be published. Thus, RS is insufficient for the conclusive determination of transition onset in $DyPO_4$. Consequently, the P_{onset} of $DyPO_4$ can be revised down to the XRD-based value of 9.1(1) GPa of this paper. Such a revision is likely not necessary for other xenotime $REPO_4$, as they already have XRD-based P_{onset} values reported in literature [9–13]. The revised $DyPO_4$ P_{onset} also marks a significant deviation from the linear dependence of

P_{onset} on RE ionic radius that is suggested in literature [4,36]. This deviation opens the intriguing possibility that, at some critical ionic radius (between those of Y^{3+} and Dy^{3+}), P_{onset} has a discontinuity, i.e., it drops from >15 GPa to < 10 GPa.

Beyond determining P_{onset} for $DyPO_4$, we find that P_{onset} is considerably stress-state dependent, with nonhydrostaticity promoting earlier transition. Neon and the mixture yield similar P_{onset} values: 9.1(1) and 9.3 GPa, respectively. The latter value can be safely understood as hydrostatic because it is lower than the hydrostatic limit of the mixture (i.e., below its freezing point). The P_{onset} difference between these two experiments is marginal and may be because they use different methods of pressure determination (the former via gold diffraction, the latter via ruby fluorescence). In contrast, the KCl experiment yields a P_{onset} of 7.0 GPa, a significant drop of ∼22%. This pressure may be even lower if the ruby pressure readings are systematically overestimated due to the nonhydrostaticity of the KCl PTM. Unlike the other PTM, KCl is a crystalline solid at all pressures [37], and it induces nonnegligible shear stresses on $DyPO_4$. This is relevant for $REPO_4$, as shown by Lacomba-Perales *et al.* [3], who report that less hydrostatic conditions result in earlier transition in YPO_4, and by Heffernan *et al.* [8], who report interesting shear-induced behaviors in $GdPO_4$. Nonhydrostaticity promoting earlier $DyPO_4$ transition is also consistent with the work of Santamaría-Pérez *et al.* [18] on orthorhombic $BaSO_4$ and gives additional insight into the mechanism of the shear-induced lowering of P_{onset} as discussed later.

When evaluating lattice parameters in this paper, it is critical to note that those of monazite are less accurate than those of xenotime, especially at pressures close to P_{onset} when the monazite signal is extremely weak. Weak monazite peaks located close to other weak monazite peaks or strong xenotime peaks can easily lead to improper LeBail fitting and introduce inaccuracy. Even in the final (highest pressure) scans of each experiment, the strongest monazite peak is weaker than the strongest xenotime peak. Despite this uncertainty, Fig. 6 shows that, across all three experiments, the monazite lattice parameters a_M, b_M, and c_M at P_{onset} are consistent. The β_M angle of the KCl experiment, however, is ∼2.5 ° higher than that of neon and the mixture (which are in close agreement).

Furthermore, the lattice parameter trends seen in the monazite phase (see Fig. 6) also exhibit some irregularities. Soon after P_{onset} in the neon experiment, a_M, b_M, and β_M trends show temporary nonmonotonicity, which is attributed to inaccurate inferred pressures rather than anomalous $DyPO_4$ behavior. At this point in the experiment, the gold peaks became extremely weak and began to overlap with stronger xenotime and neon peaks [see Fig. 3(a)]. Resultant inaccuracy in the gold peak position then propagates directly to the determined pressures. In the mixture dataset [Fig. 6(b)], at ∼10 GPa, the a_M trend becomes steeper, and the b_M and c_M trends become nonmonotonic. These irregularities coincide with the nonhydrostatic limit [10.5(5) GPa], at which point the mixture undergoes a glass transition. The KCl experiment [Fig. 6(c)] shows no contraction of the monazite unit cell due to the rather nonnegligible degrees of shear stress. This is typical of phase transitions in a high shear environment where a local drop in pressure occurs as a nucleus of the low-pressure polymorph transitions to the higher density, high-pressure polymorph. Since this localized drop will cause the transition to continue elsewhere in the sample in the absence of a hydrostatic PTM, the monazite unit cell is not expected to contract until all material is transformed.

Quantitative evaluation of these lattice parameters is further made difficult by the fact that literature does not provide lattice parameters of the high-pressure $DyPO_4$ polymorph. The best comparison point presently available is the *in situ* DAC diffraction study by López-Solano *et al.* [10] of $TbPO_4$, a neighboring composition of $DyPO_4$. Their work uses a different monoclinic cell setting than this paper; thus, their a_M is equivalent to our c_M, and their c_M is equivalent to our a_M. This switch explains why they report $a_M > c_M$, while Fig. 6 here shows the opposite. All linear (a_X, c_X, a_M, b_M, and c_M) lattice parameters reported herein are ∼1% smaller than those reported by López-Solano *et al.* [10], which is expected since Dy^{3+} has a smaller ionic radius than Tb^{3+} [1]. The monazite beta angle (β_M) reported herein is ∼3% smaller in the neon and mixture experiments and ∼1% smaller in the KCl experiment. Like $TbPO_4$, linear lattice parameters of $DyPO_4$ decrease with pressure, while β_M increases under quasihydrostatic loading. Another important structural metric is tetragonal distortion (c_X/a_X), which is plotted against pressure in Fig. S5 in the Supplemental Material [28]. The magnitude and pressure dependence of tetragonal distortion in the neon and mixture experiments is in good agreement with the $TbPO_4$ study, suggesting that xenotime $DyPO_4$ and xenotime $TbPO_4$ distort similarly under quasihydrostatic loading. Both of those PTM do not yield as great of an increase in tetragonal distortion as KCl does for the same pressure range, indicating KCl distorts xenotime $DyPO_4$ the most.

A more thorough method of assessing unit cell distortion for both xenotime and monazite is evaluating axial compressibilities (summarized in Table S1 in the Supplemental Material [28]). Analyzing relative values of axial compressibilities for a given phase provides insight into the (an)isotropic response to stress of a material. It is important to note beforehand that xenotime axial compressibilities are more accurate than monazite ones due to signal-to-noise ratio deterioration under high pressure. Heffernan [38] finds that xenotime axial compressibilities follow the order [001] ≪ [010] = [100], while monazite axial compressibilities follow [100] < [010] < [001]. Xenotime data from all three experiments as well as monazite data from the neon experiment match these trends. The mixture monazite data is not consistent because the b and c parameters no longer decrease monotonically past the hydrostatic limit. The monazite data of KCl is inconsistent because the lattice parameters appear pressure independent (i.e., the a_M, b_M, and c_M axial compressibilities are virtually 0 GPa^{-1}). This also explains why the qualities of fit for KCl monazite data (also in Table S1 in the Supplemental Material [28]) are extremely poor. Axial compressibility fits also provide zero-pressure parameters (y intercepts of the linear fits), which should be consistent with the 1 atm lattice parameters in the structure files used for LeBail fitting. Xenotime zero-pressure parameters are consistent in this respect, while monazite zero-pressure parameters are not. The inconsistency of monazite may be due to an insufficient pressure range of monazite data points, the aforementioned pressure-induced degradation of the XRD signal,

TABLE II. Bulk moduli (B_0) and their zero-pressure derivatives (B_0') calculated by fitting volume vs pressure data to the third-order Birch-Murnaghan EoS. The fits themselves are plotted in Fig. S7 in the Supplemental Material [28]. The weighted χ^2 value (χ_w^2) is the measure of goodness of fit. Fits were performed by fixing B_0' to 4.0 or by letting it float between 2.0 and 7.0. Numbers in parentheses after a value represent the standard deviation of the last digit of the value. The xenotime V_0 values marked with an asterisk are fixed during fitting. KCl monazite fits do not converge.

		$B_0' = 4$			$2 \leqslant B_0' \leqslant 7$			
Phase	PTM	V_0(Å^3)	B_0 (GPa)	χ_w^2	V_0(Å^3)	B_0 (GPa)	B_0'	χ_w^2
Xenotime	Neon	289.39(2)*	144(1)	0.05	289.39(2)*	135(1)	7.0(1)	0.03
	Mixture	289.39(2)*	170(1)	0.03	289.39(2)*	163(6)	6.4(20)	0.03
	KCl	289.39(2)*	204(18)	154.86	289.39(2)*	209(17)	2.0(40)	152.90
Monazite	Neon	266.57(70)	180(11)	0.96	267.02(75)	163(9)	6.4(22)	0.93
	Mixture	261.45(51)	421(33)	5.60	261.71(55)	389(33)	7.0(7)	4.91
	KCl	–	–	–	–	–	–	–

or the metastability of the monazite $DyPO_4$ structure used as a reference in this paper [16].

Here, *P-V* data is fit to the third-order Birch-Murnaghan EoS to explore the thermodynamics of the transition and permit comparison with elastic properties measured through other methods. EoS parameters are listed in Table II, and plots with EoS fits are shown in Fig. S7 in the Supplemental Material [28]. Two sets of fits are performed in all cases, one with B_0' fixed to four and one with B_0' floating between 2 and 7. Xenotime fits fix $V_{0,X}$ to 289.39(2) Å^3, which is derived from a precompression synchrotron scan. In monazite fits, fixing $V_{0,M}$ to the reported value of Heuser *et al.* [16] of 273.630(5) Å^3—as well as similar values reported by others [39–41]—leads to $B_{0,M}$ being lower than $B_{0,X}$. Such a finding would be inconsistent with the axial compressibility analysis performed herein, as well as prior high pressure $REPO_4$ XRD studies reporting $B_{0,M}$ to be ∼20% greater than $B_{0,X}$ in $ErPO_4$, ∼28% greater in YPO_4, and ∼6% greater in $TbPO_4$ [3,10]. Previously reported $DyPO_4$ $V_{0,M}$ values likely result in this inconsistency because they are based on metastable monazite $DyPO_4$ synthesized or simulated at 1 atm. Therefore, $V_{0,M}$ is made a free parameter in the monazite fits shown in Table II.

For the xenotime polymorph, χ_w^2 values show that the neon dataset yields qualities of fit that are like those of the mixture dataset and dramatically better than those of the KCl dataset (for both B_0' conditions). Among the neon- and mixture-based fits, the neon-based, fixed B_0' fit has the best quality (χ_w^2 closest to one) and yields a $B_{0,X}$ value that is comparable with values determined using other techniques. Namely, Wilkinson [43] reports a 122–141 GPa range using values converted from nanoindentation data, and Li *et al.* [42] report 141.5 GPa using computational chemical bond theory. Furthermore, $B_{0,X} = 144(1)$ GPa with $B_0' = 4$ is consistent with $REPO_4$ compositional trends. Even the floating B_0'-based $B_{0,X}$ is between the reported $B_{0,X}$ values of $TbPO_4$ and $HoPO_4$ (the left and right lanthanide neighbors of $DyPO_4$, respectively), which are 134 GPa ($B_0' = 6.4$) and 152 GPa ($B_0' = 4.2$), respectively [10,11].

In marked contrast, the mixture and KCl datasets give $B_{0,X}$ values that are far too high. On one hand, the exceedingly high $B_{0,X}$ values of the KCl dataset are consistent with the observations of Lacomba-Perales *et al.* [3] that nonhydrostatic DAC experiments on $REPO_4$ yield overestimated moduli. On the other hand, the high $B_{0,X}$ values of the mixture dataset cannot be explained by nonhydrostatic stress since the mixture remains hydrostatic up to ∼10.5 GPa. We suggest that this inconsistency may be because a sprinkling of Au powder was used for pressure measurement in the neon experiment, while a ruby sphere was used in the mixture and KCl experiments. While the Au powder experienced the same (quasi)hydrostatic conditions as the sample in the neon experiment, the ruby may have become trapped between the gasket and anvil in the mixture and KCl experiments. Trapping may have led the ruby to experience higher shear, resulting in a somewhat incorrect pressure reading. This explanation may be supported by close inspection of Figs. S7(c) and S7(e) in the Supplemental Material [28], which show that the xenotime EoS fits switch from lying below the experimental data to lying above the experimental data at ∼5 GPa. Considering these issues as well as the close match of the neon data with literature values as discussed above, we regard the fixed B_0' fit of the neon data as most accurate.

For the monazite polymorph, the neon dataset again yields the best fits (for both B_0' conditions), as evidenced by the respective χ_w^2 values being closer to one. The mixture dataset is significantly underfit, and most of its data points are located at pressures above the hydrostatic limit of the mixture (see Fig. S7(d) in the Supplemental Material [28]). In the mixture experiment, a similar behavior as in the KCl experiment is expected. That is, local pressure drops during nonhydrostatic compression introduce error into the fitted EoS (which naturally includes pressures >9.3 GPa for the high-pressure polymorph). The KCl monazite dataset (see Fig. S7(f) in the Supplemental Material [28]) does not produce any converging fits because $B_{0,M}$ becomes negative during optimization cycles. Taking a step back, this dataset should not yield reasonable third-order Birch-Murnaghan fits as the monazite phase is not compressed under these nonhydrostatic conditions until the entire sample volume has transitioned. Among the two neon dataset-based fits, we select the fit conducted with a fixed B_0' to have a consistent B_0' condition with the selected xenotime EoS. Therefore, we report a monazite $DyPO_4$ bulk modulus of 180(11) GPa ($B_0' = 4$) and a zero-pressure volume of 266.57(70) Å^3. This ∼25% increase from $B_{0,X}$ to $B_{0,M}$ appears consistent with the aforementioned increases in other compositions. Evaluating the value of $B_{0,M}$

itself is made difficult by the fact that no experimental comparison exists in literature—only the *ab initio* quantum chemistry calculation of 127.6 GPa by Kowalski and Li [44]. This simulated value is far lower than the $B_{0,M}$ values in Table II and even lower than the $B_{0,X}$ values reported here and elsewhere in literature [42,43]. As aforementioned, one would expect $B_{0,M}$ to be higher than $B_{0,X}$ for such $REPO_4$, as indeed is observed here. Thus, the value of Kowalski and Li [44] appears underestimated for reasons yet unknown.

It may be tempting to conclude that the neon-based $B_{0,M}$ values are as accurate if not more accurate than the neon-based $B_{0,X}$ values; however, this is not the case for two reasons: first, the $V_{0,M}$ of stable (not metastable) monazite $DyPO_4$ must be ascertained with further high-pressure XRD experiments, as this parameter has a tremendous influence on the fitted $B_{M,0}$ value. Second, even if these neon monazite data are fit using the most accurate $V_{0,M}$, $B_{M,0}$ would still be less accurate than $B_{X,0}$ due to the coexistence of xenotime and monazite phases in all scans above P_{onset}. In other words, all scans used for xenotime EoS fitting only contain xenotime, whereas all scans used for monazite EoS fitting contain both phases.

Next, we consider the mechanism of the lowered P_{onset} due to high shear in more depth. Heffernan *et al.* [8] elucidate the role of shear in $REPO_4$ structural response to pressure in their *in situ* DAC study of monazite $GdPO_4$. They observe an additional $GdPO_4$ Raman band appearing at pressures above their PTM hydrostatic limit, even though XRD suggests no such transition. The authors attribute this additional mode to shear-induced PO_4 tetrahedra distortion, which exacerbates Gd-O bond distortion [8]. Such a mechanism may also be responsible for the lower transition pressure of xenotime $DyPO_4$ in a KCl environment, as we see here. That is, hydrostatic pressure may compress the Dy-O cage, but KCl-induced shear may further distort Dy-O bonds (indirectly) via PO_4 tetrahedral distortion. The magnitude of this shear may be sufficient to not only distort Dy-O bonds, but to reconfigure them, thus triggering the early transition. Our observation of the β_M angle being $\sim 2.5^\circ$ higher in the KCl experiment than in the other experiments also points toward a possible shear-induced distortion of the monoclinic cell. Confirming this proposed mechanism will require future *in situ* DAC single-crystal XRD studies. Nevertheless, it may be scientifically interesting as well as technologically important if modifying and controlling shear could lower P_{onset} even further.

Finally, our findings can inform future $REPO_4$ work and CMC fiber coating development more broadly. Given the large discrepancy between RS- and XRD-based P_{onset} values for $DyPO_4$, XRD should be considered for conclusive P_{onset} determination in $REPO_4$ solid solutions with similar Raman band overlap (e.g., $Gd_xDy_{1-x}PO_4$). All other pure xenotime $REPO_4$—as well as $Gd_xTb_{1-x}PO_4$ and $Sm_xTb_{1-x}PO_4$ solid solutions—have already been characterized using XRD [3,10,12,13]; thus, their reported transition pressures stand unaltered. Furthermore, the at least 22% reduction of $DyPO_4$ P_{onset} under KCl loading suggests that xenotime $REPO_4$ fiber coating transformation may begin at lower pressures than expected in the high-shear environment of a CMC. This in turn means that transformation-based plasticity and toughening mechanisms could be activated at lower stresses in the application environment. Therefore, the propensity of a candidate material for transformation should be assessed under high-shear—in addition to hydrostatic—conditions. Using shear-sensitivity as a criterion for screening $REPO_4$ candidates potentially opens a wider range of compositions worth considering for CMC applications.

V. CONCLUSIONS

This experimental paper provides crystallographic proof that xenotime $DyPO_4$ transitions directly to the monazite structure upon room temperature compression. Prior RS indicated a transition onset pressure of 15.3 GPa [14]; however, our synchrotron XRD study shows that transition onset is much earlier, at 9.1 GPa. All lattice parameters and their pressure dependences are consistent with the trends reported for the neighboring $TbPO_4$ composition. By employing neon, 16:3:1 methanol-ethanol-water, and KCl as PTM, we also explored the effect of various levels of hydrostaticity on the phase behavior, finding that nonhydrostaticity reduces P_{onset} to at least as low as 7.0 GPa. Compared with the other PTM, KCl causes the most rapid increase in the xenotime c/a ratio and yields the highest monazite β angle. These are both likely indicators of shear-induced structural distortion of the PO_4 tetrahedra, which may have triggered the early phase transition. For all PTM, xenotime and monazite coexist for large pressure ranges, suggesting that this transition is kinetically limited. Calculated axial compressibilities reveal the anisotropy of $DyPO_4$ response to stress and are consistent with expectations for $REPO_4$ in general. Our third-order Birch-Murnaghan EoS fits of (quasi)hydrostatic data yield a xenotime bulk modulus of 144(1) GPa and a monazite bulk modulus of 180(11) GPa (both with B_0' fixed to four). The findings presented herein provide additional insight into the pressure-induced transition in $DyPO_4$ and how this transition could be tailored to CMC fiber coating applications.

ACKNOWLEDGMENTS

The authors thank Dr. Jesse Smith and Dr. Ross Hrubiak for performing initial alignments at the beamline, Dr. Sergey Tkachev for assisting with gas-loading samples, as well as Sarah Boardman and Dr. Yachao Chen for helping perform the beamline experiments. The authors also thank Dr. Nitin Kumar and Dr. Sina Soltanmohammed, who assisted in developing the batch-processing and batch-fitting procedures for the synchrotron data. J.S. was supported by the Department of Defense through the National Defense Science & Engineering Graduate Fellowship Program. B.H. was supported by resources at the Spallation Neutron Source and the High Flux Isotope Reactor, Department of Energy (DOE) Office of Science User Facilities operated by the Oak Ridge National Laboratory. This work was performed at HPCAT (Sector 16), Advanced Photon Source, Argonne National Laboratory. HPCAT operations are supported by DOE National Nuclear Security Administration under Award No. DE-NA0001974 and DOE Office of Basic Energy Sciences (BES) under Award No. DE-FG02-99ER45775, with partial instrumentation funding by the National Science Foundation (NSF). Use of the COMPRES-GSECARS gas-loading system was supported by COMPRES under NSF Cooperative Agreement No. EAR

11–57758 and by GSECARS through NSF Grant No. EAR-1128799 and DOE Grant No. DE- FG02-94ER14466. A.P.S. is supported by DOE-BES, under Contract No. DE-AC02-06CH11357. This research was funded by the NSF under Award No. DMR-1352499.

This manuscript has been authored by UT-Battelle, LLC under Contract No. DE-AC05-00OR22725 with the U.S. Department of Energy. The U.S. Government retains, and the publisher, by accepting the article for publication, acknowledges that the U.S. Government retains a nonexclusive, paid-up, irrevocable, worldwide license to publish or reproduce the published form of this manuscript, or allow others to do so, for U.S. Government purposes. The Department of Energy will provide public access to these results of federally sponsored research in accordance with the DOE Public Access Plan [45].

[1] L. A. Boatner, Rev. Miner. Geochem. **48**, 87 (2002).
[2] S. V. Ushakov, K. B. Helean, A. Navrotsky, and L. A. Boatner, J. Mater. Res. **16**, 2623 (2001).
[3] R. Lacomba-Perales, D. Errandonea, Y. Meng, and M. Bettinelli, Phys. Rev. B **81**, 064113 (2010).
[4] R. S. Hay, P. Mogilevsky, and E. Boakye, Acta Mater. **61**, 6933 (2013).
[5] P. J. Meschter, U.S. Patent No. US 2010/0069226 A1 (18 March 2010).
[6] R. S. Hay, E. E. Boakye, P. Mogilevsky, G. E. Fair, T. A. Parthasarathy, and J. E. Davis, J. Am. Ceram. Soc. **96**, 1586 (2013).
[7] E. Stavrou, A. Tatsi, E. Salpea, Y. C. Boulmetis, A. G. Kontos, Y. S. Raptis, and C. Raptis, J. Phys. Conf. Ser. **121**, 042016 (2008).
[8] K. M. Heffernan, N. L. Ross, E. C. Spencer, and L. A. Boatner, J. Solid State Chem. **241**, 180 (2016).
[9] A. Tatsi, E. Stavrou, Y. C. Boulmetis, A. G. Kontos, Y. S. Raptis, and C. Raptis, J. Phys. Condens. Matter **20**, 425216 (2008).
[10] J. López-Solano, P. Rodríguez-Hernández, A. Munoz, O. Gomis, D. Santamaría-Perez, D. Errandonea, F. J. Manjón, R. S. Kumar, E. Stavrou, and C. Raptis, Phys. Rev. B **81**, 144126 (2010).
[11] O. Gomis, B. Lavina, P. Rodríguez-Hernández, A. Muñoz, R. Errandonea, D. Errandonea, and M. Bettinelli, J. Phys. Condens. Matter **29**, 095401 (2017).
[12] F. X. Zhang, M. Lang, R. C. Ewing, J. Lian, Z. W. Wang, J. Hu, and L. A. Boatner, J. Solid State Chem. **181**, 2633 (2008).
[13] F. X. Zhang, J. W. Wang, M. Lang, J. M. Zhang, R. C. Ewing, and L. A. Boatner, Phys. Rev. B **80**, 184114 (2009).
[14] M. A. Musselman, T. M. Wilkinson, B. Haberl, and C. E. Packard, J. Am. Ceram. Soc. **101**, 2562 (2018).
[15] E. Stavrou, A. Tatsi, C. Raptis, I. Efthimiopoulos, K. Syassen, A. Munoz, P. Rodríguez-Hernández, J. López-Solano, and M. Hanfland, Phys. Rev. B **85**, 024117 (2012).
[16] J. M. Heuser, S. Neumeier, L. Peters, H. Schlenz, D. Bosbach, and G. Deissmann, J. Solid State Chem. **273**, 45 (2019).
[17] D. Errandonea, Y. Meng, M. Somayazulu, and D. Häusermann, Phys. B Condens. Matter **355**, 116 (2005).
[18] D. Santamaría-Pérez, L. Gracia, G. Garbarino, A. Beltrán, R. Chuliá-Jordán, O. Gomis, D. Errandonea, C. Ferrer-Roca, D. Martínez-García, and A. Segura, Phys. Rev. B **84**, 054102 (2011).
[19] R. Hrubiak, S. Sinogeikin, E. Rod, and G. Shen, Rev. Sci. Instrum. **86**, 072202 (2015).
[20] M. Rivers, V. B. Prakapenka, A. Kubo, C. Pullins, C. M. Holl, and S. D. Jacobsen, High Press. Res. **28**, 273 (2008).
[21] S. V. Sinogeikin, J. S. Smith, E. Rod, C. Lin, C. Kenney-Benson, and G. Shen, Rev. Sci. Instrum. **86**, 072209 (2015).
[22] A. Dewaele, P. Loubeyre, and M. Mezouar, Phys. Rev. B **70**, 094112 (2004).
[23] F. Birch, J. Appl. Phys. **9**, 279 (1938).
[24] H. K. Mao, J. Xu, and P. M. Bell, J. Geophys. Res. **91**, 4673 (1986).
[25] C. Prescher and V. B. Prakapenka, High Press. Res. **35**, 223 (2015).
[26] T. Degen, M. Sadki, E. Bron, U. König, and G. Nénert, Powder Diffr. **29**, S13 (2014).
[27] J. Gonzalez-Platas, M. Alvaro, F. Nestola, and R. Angel, J. Appl. Crystallogr. **49**, 1377 (2016).
[28] See Supplemental Material at http://link.aps.org/supplemental/10.1103/PhysRevB.103.184105 for Figs. S1–S7 (additional XRD- and Raman-based plots) as well as Table S1 (axial compressibilities).
[29] A. Le Bail, Powder Diffr. **20**, 316 (2005).
[30] W. O. Milligan, D. F. Mullica, G. W. Beall, and L. A. Boatner, Inorganica Chim. Acta **70**, 133 (1983).
[31] L. W. Finger, R. M. Hazen, G. Zou, H. K. Mao, and P. M. Bell, Appl. Phys. Lett. **39**, 892 (1981).
[32] R. J. Hemley, C. S. Zha, A. P. Jephcoat, H. K. Mao, L. W. Finger, and D. E. Cox, Phys. Rev. B **39**, 11820 (1989).
[33] S. Klotz, J.-C. Chervin, P. Munsch, and G. Le Marchand, J. Phys. D. Appl. Phys. **42**, 075413 (2009).
[34] S. Froyen, and M. L. Cohen, J. Phys. C Solid State Phys. **19**, 2623 (1986).
[35] J. W. Gibbs, *Scientific Papers: Thermodynamics* (Dover Publications, New York, 1961), Vol. 1.
[36] M. A. Musselman, Master's thesis, Colorado School of Mines (2017).
[37] A. Dewaele, A. B. Belonoshko, G. Garbarino, F. Occelli, P. Bouvier, M. Hanfland, and M. Mezouar, Phys. Rev. B **85**, 214105 (2012).
[38] K. M. Heffernan, Ph.D. thesis, Virginia Tech (2016).
[39] M. Kizilyalli and A. J. E. Welch, J. Appl. Crystallogr. **9**, 413 (1976).
[40] Y. Hikichi, T. Sasaki, S. Suzuki, K. Murayama, and M. Miyamoto, J. Am. Ceram. Soc. **71**, C-354 (1988).
[41] A. Blanca Romero, P. M. Kowalski, G. Beridze, H. Schlenz, and D. Bosbach, J. Comput. Chem. **35**, 1339 (2014).
[42] H. Li, S. Zhang, S. Zhou, and X. Cao, Inorg. Chem. **48**, 4542 (2009).
[43] T. M. Wilkinson, Ph.D. thesis, Colorado School of Mines (2017).
[44] P. M. Kowalski and Y. Li, J. Eur. Ceram. Soc. **36**, 2093 (2016).
[45] http://energy.gov/downloads/doe-public-access-plan